1996ApJ...456..651G

THE ASTROPHYSICAL JOURNAL, 456:651-661, 1996 January 10

K4-55: A BIPOLAR PLANETARY NEBULA OBSERVED NEAR POLE-ON

M. A. GUERRERO,[1] A. MANCHADO,[1] AND M. SERRA-RICART
Instituto de Astrofisica de Canarias, E-38200 La Laguna (Tenerife), Spain; mar@ll.iac.es, amt@ll.iac.es, mserra@ll.iac.es
Received 1995 April 10; accepted 1995 July 18

ABSTRACT

A comprehensive study of the planetary nebula K4-55 is presented. In addition to CCD narrowband images, spatially resolved low-dispersion and high-resolution spectra were obtained. This has allowed the different morphological features in the images to be connected with the kinematics and with the physical information, leading to the establishment of the complex nebular structure.

K4-55 is a new multiple-shell planetary nebula displaying three different parts: a faint halo that extends up to 2′ from the main nebula; an outer part revealed by the kinematical study as a pole-on bipolar structure; and an inner, bright ring. The bipolar structure is expanding at ~ 100 km s^{-1} at the poles, while the halo has $V_{\rm exp} \lesssim 8.6$ km s^{-1}. The inner ring exhibits intriguing kinematics, indicating a likely presence of rotation. Abundance variations are found throughout the nebula, with a N/O abundance ratio enhancement in the [N II]-bright central ring, whereas the extended halo presents a much smaller ratio. The N/O ratio reported is among the highest ever found in planetary nebulae. The outer halo is consistent with the asymptotic giant branch wind, whereas the inner nebula was formed during a later mass-loss phase.

Subject headings: ISM: abundances — ISM: kinematics and dynamics — ISM: structure — planetary nebulae: individual (K4-55)

1. INTRODUCTION

Extended halos or multiple shells are a widespread phenomenon (Jewitt, Danielson, & Kupferman 1986; Chu, Jacoby, & Arendt 1987; Manchado & Pottasch 1989; Balick et al. 1992) in planetary nebulae (hereafter PNs). However, triple-shell structure has been observed in only nine PNs: those listed in Chu et al. (1991), NGC 3587 (Manchado et al. 1993), and K4-55 (this paper). The study of this kind of object provides a direct method to compare the nebular morphology and chemical properties with the predicted stellar evolution models.

Current intermediate-mass stellar evolution models, e.g., Iben & Renzini (1983), predict a slow, steady mass-loss rate during the asymptotic giant branch (AGB) phase and a later superwind phase lasting ~ 1000 yr, which forms the PN. Vassiliadis & Wood (1993) recently developed evolutionary stellar tracks on the AGB phase, which include mass loss via an empirical law relating the mass-loss rate to the pulsation period of OH/IR stars and Mira variables. According to this work, most AGB stars probably experience several discrete superwind phases, offering a natural explanation for the detached multiple-shell PNs observed in the Galaxy (Chu et al. 1987). By studying the kinematics of the different shells, it is possible to compare their lifetimes with those predicted by the theory. Furthermore, during those late epochs of stellar evolution, several dredge-up stages take place (e.g., Becker & Iben 1980; García-Berro & Iben 1994), bringing heavy elements to the star's surface, which are later expelled to the nebula. Therefore, a spatially resolved study of the abundances within the nebula will allow these different episodes of dredge-up to be traced.

Since Kohoutek classified K4-55 (PK 084+1°1) as a possible planetary nebula in 1972, only limited study has been carried out on this particular object. The initial research work on K4-55 was directed toward proving that it was really a PN (Sabbadin 1986). The previous single-aperture spectroscopic data (Acker et al. 1992) show a very reddened PN ($c_{\rm H\beta} = 1.3$) with strong emission in the [N II] lines. The red POSS plate shows an irregular and moderately extended object.

Within the morphological survey of northern sky PNs (Manchado et al. 1996), in progress at the IAC, CCD images of K4-55 have been obtained through narrowband filters centered on the Hα + [N II] and [O III] emission lines. Since they revealed a multiple-shell structure, the nebula was included in our program to study differential abundances and kinematics in PNs. Hence, long-slit low-dispersion spectra were obtained at different positions of the nebula in an attempt to investigate the chemical composition of the ionized gas. Furthermore, spatially resolved high-resolution spectroscopy was carried out to study the gas kinematics.

This paper reports on the results of our imagery and high- and low-resolution spectroscopic data of the nebula K4-55. The observations are described in § 2. The morphology, kinematic properties, and physical conditions and abundances are explained in §§ 3, 4, and 5, respectively. An estimate of the distance to the nebula is given in § 6. Finally we present a discussion in § 7 and a brief conclusion in § 8.

2. OBSERVATIONS AND DATA REDUCTION

2.1. *Narrowband Images*

The CCD images of K4-55 were obtained using the 0.8 m telescope (IAC80) at the Observatorio del Teide (Tenerife) in 1993 November, during commissioning time, and the 2.54 m Nordic Optical Telescope (NOT) at the Observatorio del Roque de los Muchachos (La Palma) in 1994 April. A 1024 × 1024 Thomson CCD with a pixel size of 20 μm was employed in both observations. The filters utilized in the observations have the following properties: the Hα + [N II]

---

[1] Visiting Astronomer, German-Spanish Astronomical Centre, Calar Alto, operated by the Max-Planck-Institut für Astronomie, Heidelberg, jointly with the Spanish National Commission for Astronomy.

TABLE 1

ECHELLE OBSERVATIONS AND LOW-RESOLUTION SPECTROSCOPY OF K4-55

Slit Position	Telescope and Instrument	Spectral Range	Offset from Central Position	Position Angle	Exposure Time (minutes)
1........	WHT (UES)	6500–6600	0	0°	30
2........	WHT (UES)	6500–6600	0	90	45
3........	CAHA (TCS)	3650–5250	0	90	60
3........	CAHA (TCS)	5700–7350	0	90	60
4........	CAHA (TCS)	3650–5250	8″ N	90	25
4........	CAHA (TCS)	5700–7350	8″ N	90	20

filter has a central wavelength of 6563 Å, with a FWHM of 100 Å, while the [O III] filter was centered at 5008 Å with a FWHM of 30 Å.

At the IAC80 telescope, pixel size corresponds to 0″.435, and the field of view is $\sim$7′. Six images of 900 s were taken through the Hα + [N II] filter. The average image is shown in Figure 1 (Plate 22) and is presented at two levels to accentuate the bright and faint features. At the NOT, the pixel size was 0″.14, so the field was $\sim$2′.4. Three images of 900 s were taken through the [O III] filter. The average is presented in Figure 2 (Plate 23). The seeing was less than or equal to 1″.7 throughout the observations.

Standard CCD reduction techniques such as bias subtraction and flat-field correction were applied to all the frames using the IRAF[2] (Image Reduction and Analysis Facility) tasks.

2.2. *Echelle Observations*

High-resolution long-slit spectra were obtained in order to investigate the internal motion of the different features and the radial velocity of the whole nebula. The Utrecht Echelle Spectrograph (UES) on the 4.2 m William Herschel Telescope at the Observatorio del Roque de los Muchachos (La Palma) was used during a run in 1993 August.

We utilized the 79 line mm^{-1} echelle grating and a 700 mm focal length camera. The observations were taken through a narrowband filter which isolates the Hα λ6563 and [N II] λ6548 and λ6584 lines in the 34th echelle order. The slit used was 1″.1 wide and 200″ in length. The spatial scale on the detector, a Tektronix CCD (1024 × 1024 pixel^2 of 24 μm size each), is 0″.72, given that an on-chip binning by a factor of 2 in the spatial direction was applied. The reciprocal dispersion was 2.92 Å mm^{-1} at 6560 Å, equivalent to 3.21 km s^{-1} pixel^{-1}. The instrumental FWHM was 6.9 ± 0.3 km s^{-1}.

Two long-slit echelle spectra were obtained passing through the center of the main nebula in the S-N and E-W directions. The slit positions, orientations, and exposure times are given in Table 1. The slit positions are also shown in Figure 1. Standard calibration lamp spectra were used to rebin the data to a linear wavelength scale and to remove curvature along the slit length. A Th-Ar arc lamp was used to calibrate the data. Spatial and velocity calibrated gray-scale images of the spectra in the Hα λ6562.85 and [N II] λ6583.37 lines are reproduced in Figure 3 (Plate 24) for the two slit positions (see legend).

2.3. *Low-Dispersion Spectroscopic Observations*

To determine the physical conditions and chemical abundances of the ionized gas in this object, we obtained long-slit low-dispersion spectra by means of the Cassegrain Twin-Spectrograph (CTS) on CAHA's 3.5 m telescope at Calar Alto (Almeria) during 1993 July and 1994 October. This instrument includes two separate spectroscopic channels (*blue* and *red*) that allow intermediate spectral resolution data to be obtained from λ3500 to λ7350 operating simultaneously with two CCD detectors, one for each channel. Identical Tektronix CCDs to that employed in the echelle observations were utilized in both spectrograph's arms. The slit was 1″.2 wide and 4′ long. The blue T08 and red T04 grisms, both with 600 line mm^{-1}, gave a reciprocal dispersion of 72 Å mm^{-1}. The effective spectral resolution was 3.5 Å, and the spatial resolution was 0″.9.

The slit positions, orientations, and exposure times are given in Table 1. The slit positions for the spectroscopic observations are also shown on the Hα + [N II] image (Fig. 1).

3. MORPHOLOGY OF K4-55

The Hα + [N II] and [O III] images of K4-55 are presented in Figures 1 and 2, respectively. The Hα + [N II] image reveals a bright inner ring and two diametrically opposed peculiar armlike structures protruding from the eastern and western parts of the central ring and extending up to 30″. The inner part consists of a smooth hollow ellipse (12″ × 10″) where no central star is present (at the detection limit). There is a break north of the ring, and the western part appears to be thicker than the eastern one. Emission from the inner part of the ring is $\sim$20% of that of the ring. Two spiral features arise from the southease and northwest of the inner ring and swirl clockwise. They are patchy and knotty, finishing as irregular filaments. The southeast emission has a faint counterpart at the northeast, so it resembles a limb-brightened thin lobe extending 40″ east of the inner part. This is uncertain in the western part, but it would allow us to explain the emission extending up to 25″ from the center of the nebula as the emission that fills the hypothetical western lobe. More observations are needed in order to confirm this last point, but the idea is supported by long-slit observations that detect faint emission ($\lesssim$2% peak) up to 50″ from the center of the nebula both in the eastern and the western directions. An interesting detail is that the armlike features can be interpreted as the result of point symmetrical distribution of the emission, which is also observed in other bipolar PNs (e.g., NGC 6309; Balick 1987).

Although an additional faint halo is detected, both in high- and low-resolution spectroscopy (see below), it eludes detection in our direct images.

The image in [O III] λ5007 (Fig. 2) is very poor, owing in part to the high extinction of this object ($c_{\mathrm{H}\beta} = 1.3$). Never-

---

[2] IRAF is distributed by the National Optical Astronomy Observatories, which is operated by the Association of Universities for Research in Astronomy, Inc. (AURA) under cooperative agreement with the National Science Foundation.

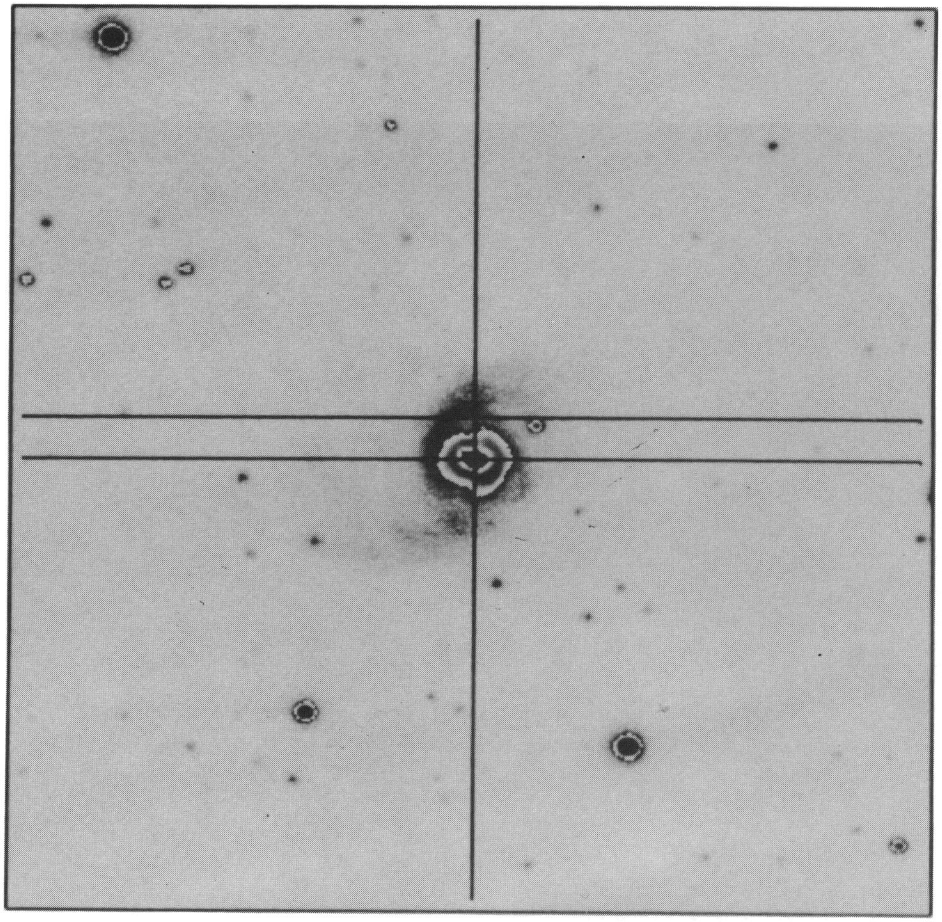

FIG. 1.—CCD image of K4-55 taken through a filter in the Hα + [N II] lines displaying the bright nebular core at a different brightness scale from the much fainter lobes in order to show the structure in both regions. The slit positions for the echelle and low-resolution spectra are marked. According to Table 1, vertical slit is position 1, lower horizontal slit is positions 2 and 3, and upper horizontal slit is position 4. The field of view is 3′.

GUERRERO, MANCHADO, & SERRA-RICART (see 456, 652)

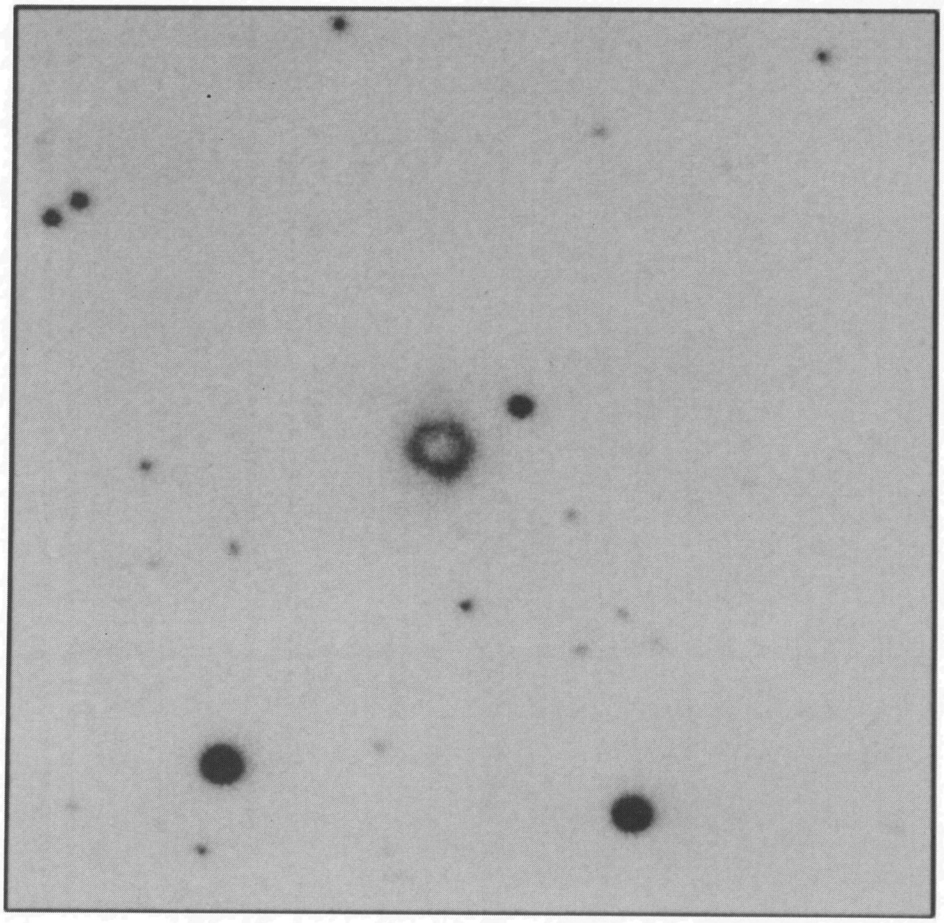

FIG. 2.—CCD image of K4-55 taken through a narrow filter in the [O III] λ5007 line. The image is 143 × 143 arcsec^2.

GUERRERO, MANCHADO, & SERRA-RICART (see 456, 652)

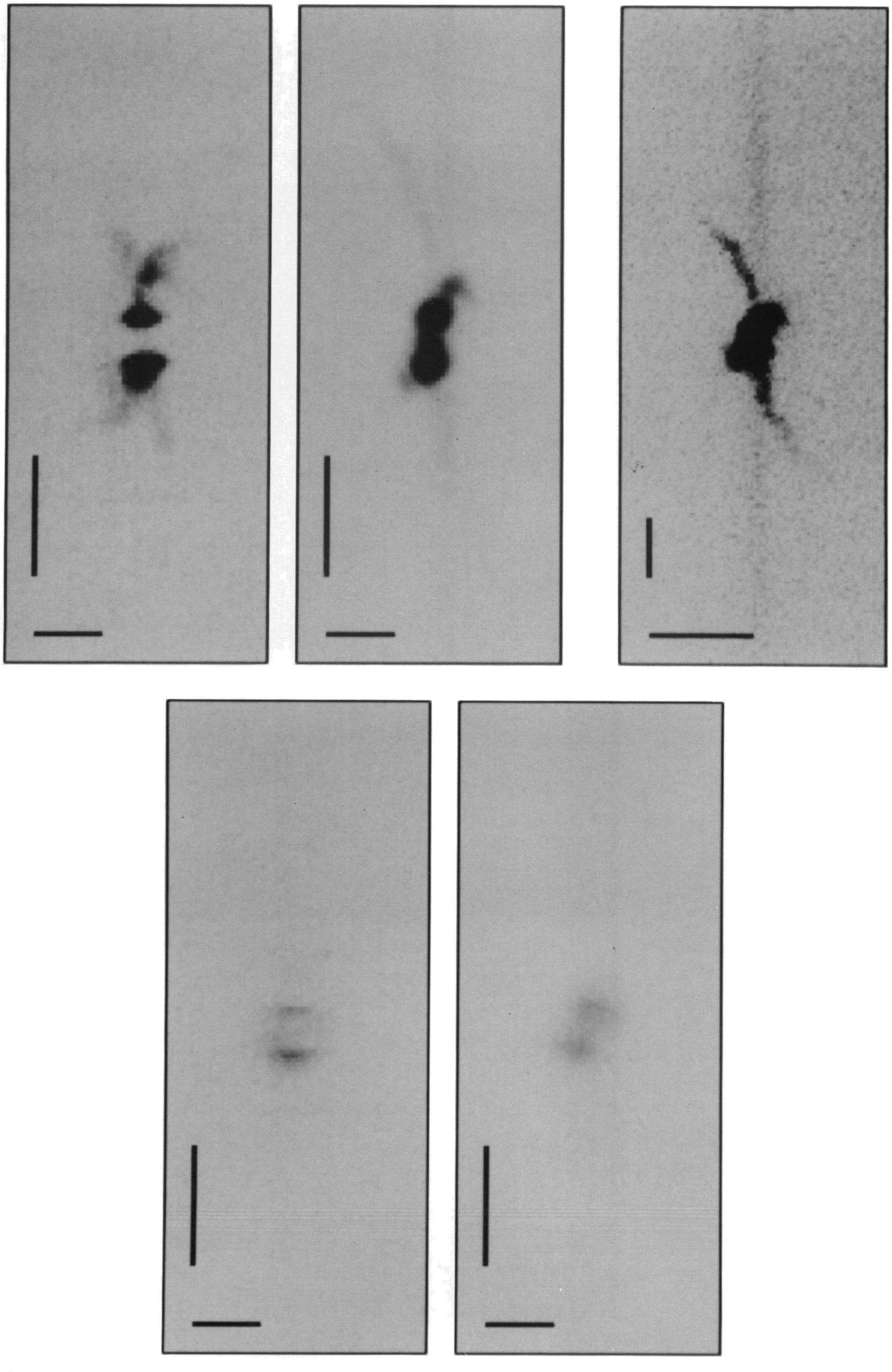

FIG. 3.—*Top:* [N II] λ6584 echellogram at the position angle 0° (*left*) and 90° (*center*), showing the kinematical behavior of the main nebula. The vertical bar is equivalent to 30″. *Right:* the whole slit at position angle 90°, displayed at an intensity level that shows the halo, although the main nebula is showed overexposed. The vertical bar is equivalent to 60″. *Bottom:* Hα λ6563 line image taken from the echelle at position angle 0° and 90° respectively. The vertical bar is equivalent to 30″. The horizontal bar is equal to 100 km s^{-1} in all the images.

1996ApJ...456..651G

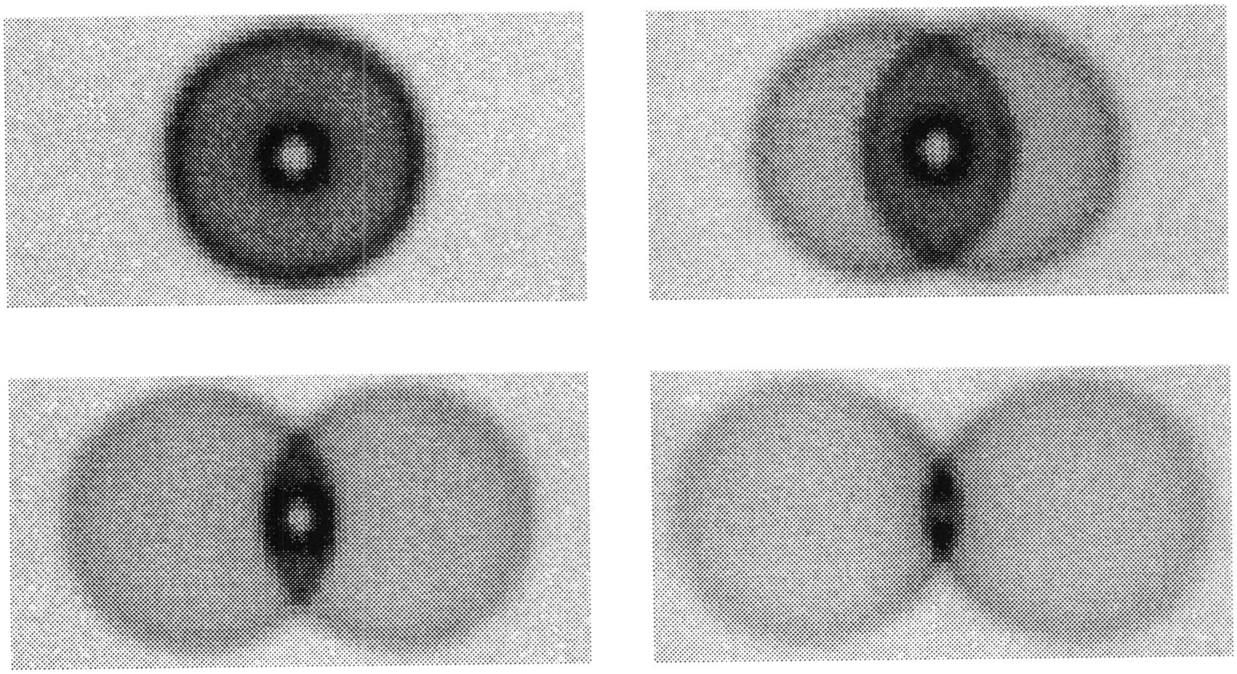

FIG. 10*a*

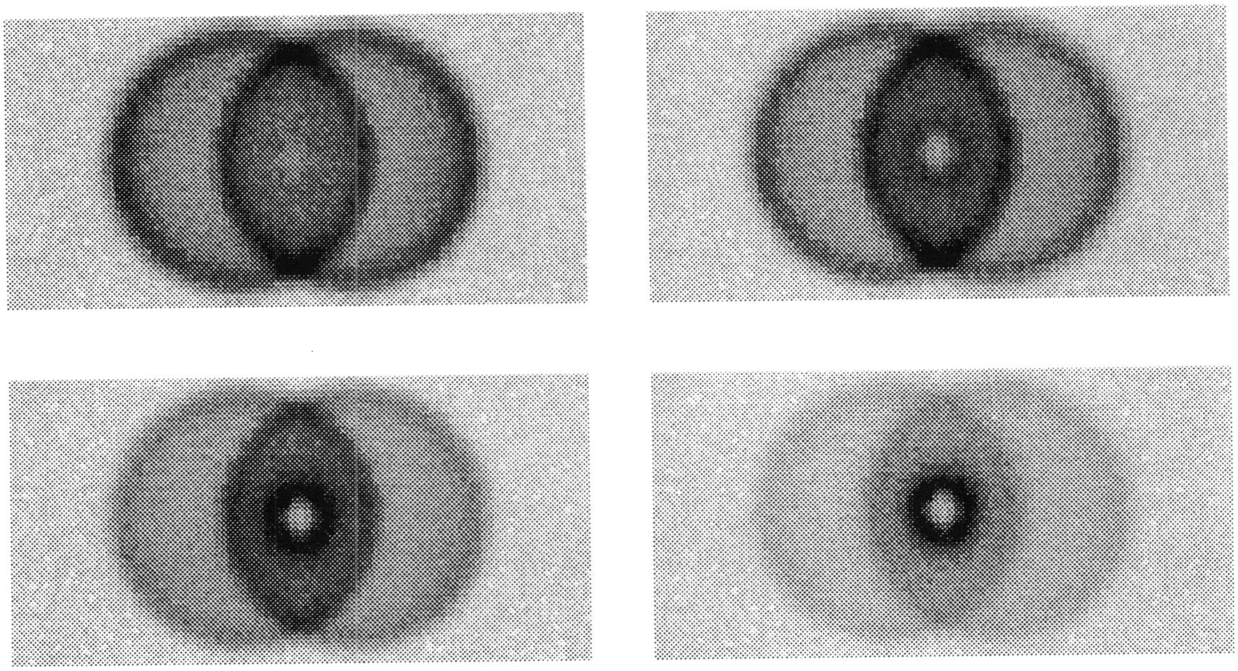

FIG. 10*b*

FIG. 10.—(*a*) Synthetic images obtained by projecting a simple model of a bipolar planetary nebula (Solf & Ulrich 1985) over the plane of the sky. The exponent for the emission law is the same ($\xi = 2.5$), but the inclination differs, namely 0° (*upper left*), 20° (*upper right*), 40° (*lower left*), and 60° (*lower right*). Comparison with the image taken through the Hα + [N II] filter yields a value for the inclination between 20° and 40° and nearer to 20°. (*b*) The same as (*a*), but the inclination is now fixed at 20°, and the exponent (ξ) for the emission law has been changed. The values considered are 1.0 (*upper left*), 2.0 (*upper right*), 2.5 (*lower left*), and 3.0 (*lower right*). The larger values of ξ seem to give the best fit to the data. Therefore, the tops of the bipolar lobes are very faint, even suggesting that the lobes could be opened.

GUERRERO, MANCHADO, & SERRA-RICART (see 456, 652)

theless, it indicates that no high-excitation gas exists outside the central ring. The difference between the central part of the nebula and the ring is not so conspicuous (former emission is ~35% that of the ring) as in the Hα + [N II] image, revealing likely differences in excitation.

4. KINEMATIC PROPERTIES OF K4-55

The [N II] λ6584 line is used to obtain the position versus velocity plots, because it is the strongest line in the object and, furthermore, it is little affected by thermal broadening. Radial velocities, corrected to the local standard of rest, against equatorial coordinates plots are presented in Figure 4 for the two slit positions. From these, we can obtain information about the internal motion of the different features and the radial velocity of the whole nebula.

The outermost feature extends along the whole slit, as can be seen in the E-W oriented slit (Fig. 4 [*top*]). Its radius is then up to 100″, which is the extension of the slit. The velocity at the position nearest to the central part of the nebula is ~2 km s^{-1}, but as the offset from the central part increases, the velocity decreases to ~0 km s^{-1}. This might indicate that the interaction of the faint halo around the nebula is taking place with the ambient medium. The emission is not split. However, an attempt was made in order to estimate an upper limit to the possible expansion. As the measured FWHM of the line profile, $W_{\rm m}$, is due to the convolution of thermal, instrumental, turbulent, and expansion components, it can be approximated as

$$W_m^2 = W_{\rm th}^2 + W_{\rm ins}^2 + W_{\rm tur}^2 + W_{\rm exp}^2 . \qquad (1)$$

If we assume T_e to be equal to 10,000 K, the resulting value for $W_{\rm th}$ is 5.7 km s^{-1}. The instrumental FWHM, $W_{\rm ins}$, was 6.9 km s^{-1}. Taking into account that the FWHM measured was 0.43 Å, which means 19.6 km s^{-1}, the contribution of turbulence and expansion to the total FWHM is 17.3 km s^{-1}. If the halo were a simple, spherically expanding shell, the expansion contribution at the center would be two components separated in velocity by 2 × $V_{\rm exp}$. Under the assumption that the turbulence component is zero, it gives us an upper limit for the expansion of ~8.6 ± 1.0 km s^{-1}.

As described in § 3, the bright central part is surrounded by two armlike structures. The echelle observations separate each of them into two different kinematical features, one approaching and the other receding. In the E-W slit (Fig. 4 [*top*]), the λ6584 [N II] line diverges into two velocity components outside the inner ring (offset up to 10″). One of the velocity components extends only a few arcseconds and reaches ~25 km s^{-1}. The more extended component extends up to 35″ from the center of the nebula, the velocity range over the nebula being 90 km s^{-1}. The emission from these features is brighter (Fig. 3 [*top*]) than that from the outermost parts (halo). Figure 4 (*bottom*) shows the position versus velocity plot of the S-N oriented long-slit echelle. In this case, velocity components are equally extended (20″ from the center) and move at similar velocities ($\lesssim 20$ km s^{-1}), although in opposite directions.

Similar behavior has been reported to exist in other PNs (e.g., NGC 2440) and is explained as bipolar expansion (Schwarz 1993). In addition, our E-W echelle data can be compared qualitatively with the synthetic lines presented in Icke, Preston, & Balick (1989), confirming that K4-55 is a bipolar PN.

The central part, a hollow bright emission ring, exhibits remarkably dissimilar behavior at each slit position. In the E-W slit, there is a difference of ~5 km s^{-1} between the western and eastern parts of the inner ring, with the former approaching the observer. A velocity gradient exists from the east to the west, except at the centermost part, where a velocity dip is present on the velocity-position plot. The average radial velocity measured from the inner emission is $V_{\rm LSR}$ ~ −2 km s^{-1}, differing from the halo velocity by 4 km s^{-1}. In the S-N slit, the measured velocity varies abruptly at the central position of the ring, where it changes from −3 to 3 km s^{-1}. As we move toward the edge of the region, the differences in velocity

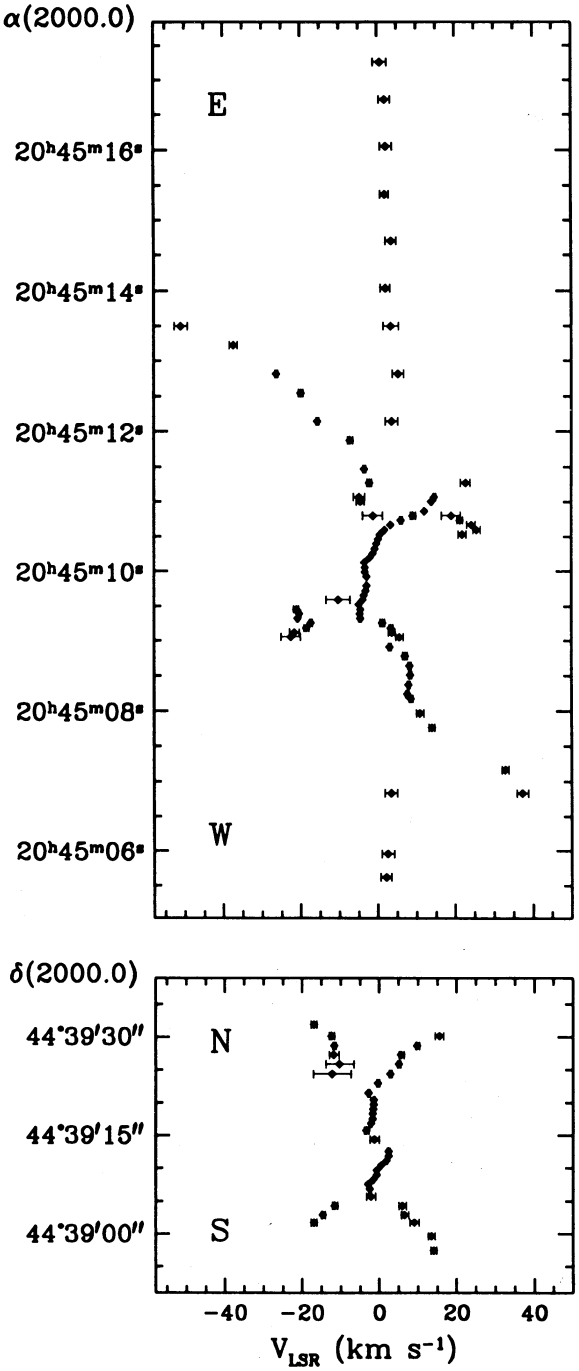

FIG. 4.—Velocity vs. position plots from the [N II] λ6584 line. Error estimates in the velocity determination are shown.

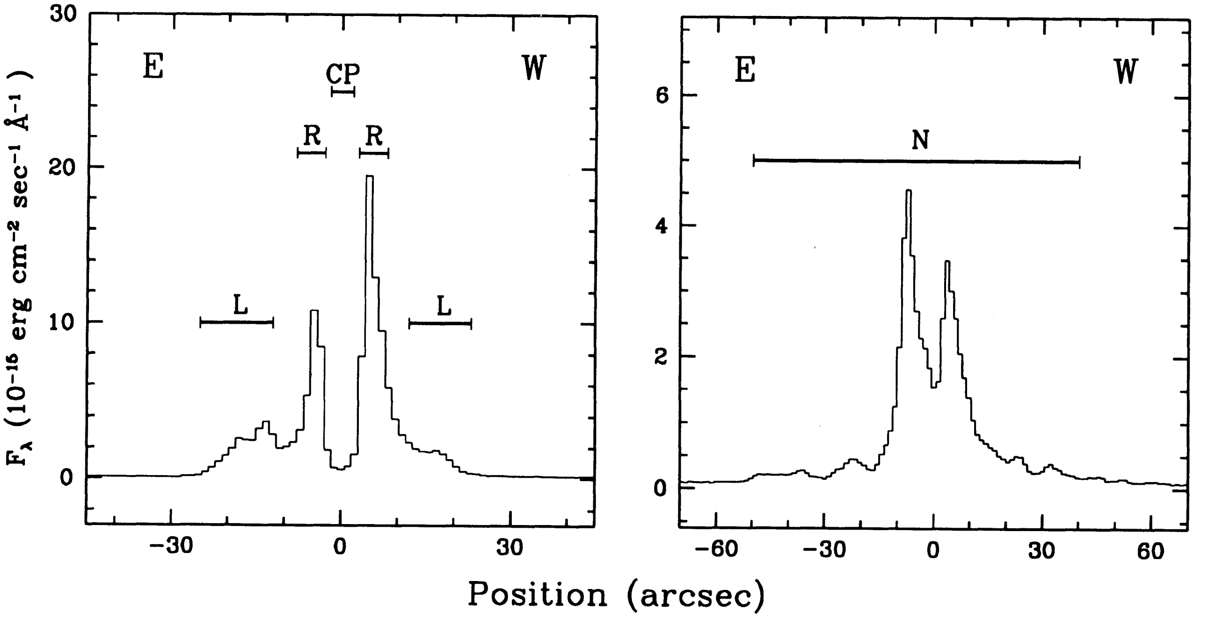

FIG. 5.—Surface brightness profiles in the [N II] line extracted from the low-dispersion spectra for the slit passing through the central position of the nebula (*left*) and for the slit in the northern position (*right*). In both positions, the halo extends up to 2′ west and east of the brightest parts.

between the north and south parts decrease, its outer parts exhibiting similar velocities (∼ −2 km s^{-1}).

5. PHYSICAL CONDITIONS AND ABUNDANCES OF K4-55

5.1. *Spectral Analysis*

From the two spatially resolved, low-resolution, long-slit spectra obtained, we grouped together spectra presenting similar characteristics and that are related with the different morphological and kinematic features of the PN. Five averaged spectra were extracted. Their locations are labeled against the [N II] λ6584 surface brightness profiles in Figure 5. According to the morphological features described in § 3, CP (∼4″) corresponds to the hollow part of the inner ring, R (∼10″) to the inner ring, L (∼25″) to the lobes, and N (∼50″) to the lobes' emission enhancement observed north of the inner ring. The size of the ring is ∼10″, the almost hollow central part extending along a radius up to 2″. The lobes emission reaches up to 25″. The faint emission of the halo appears in both slit positions and extends up to 2′.0 from the center of the main nebula. We averaged it in a one-dimensional spectrum (region H).

The individual spectra of those regions are shown in Figures 6 and 7. The red spectra show the Hα, [N II], and [S II] lines separately, in order to point out how the relations among these lines change in the different regions. In particular, the high [N II] to Hα ratio in the ring is remarkable . The spectrum of the central region shows emission lines from high ionization states ([Ne IV], [Ar IV], [Ar V]), in addition to the brightest He II lines. Emission from the lobes and halo is very dim. The absorptions present in these spectra toward λ3950 are associated to sky subtraction problems because of the weakness of the spectra.

We have derived the extinction in the regions where the signal-to-noise ratio is highest, using the theoretical Balmer lines ratios (Brocklhurst 1971), adopting case B recombination ($T_e = 10^4$ K and $N_e = 10^4$ cm^{-3}) and using the standard

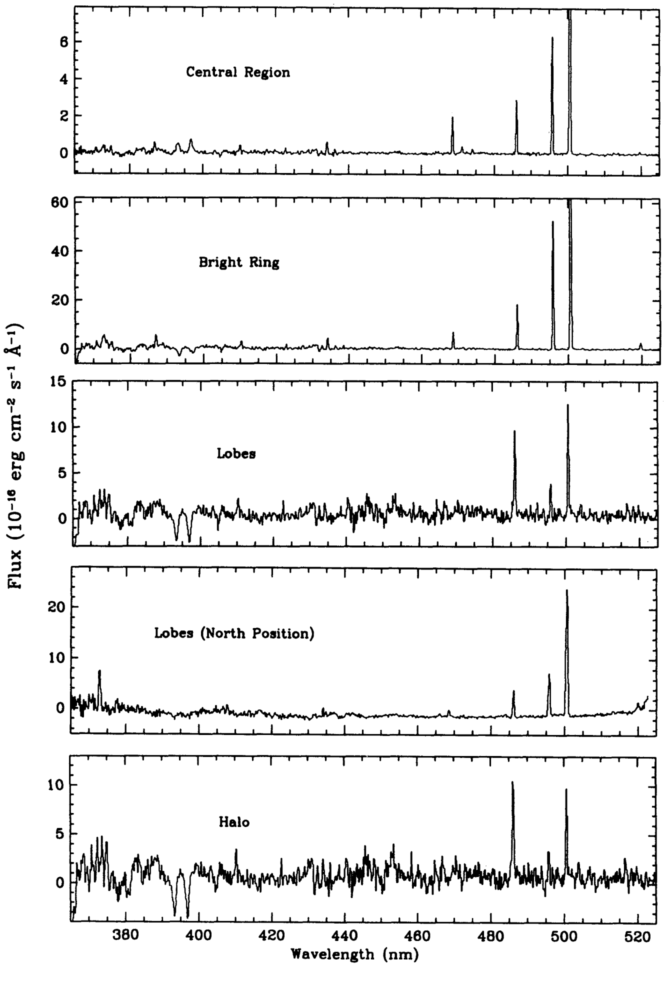

FIG. 6.—Blue spectra of the different regions considered

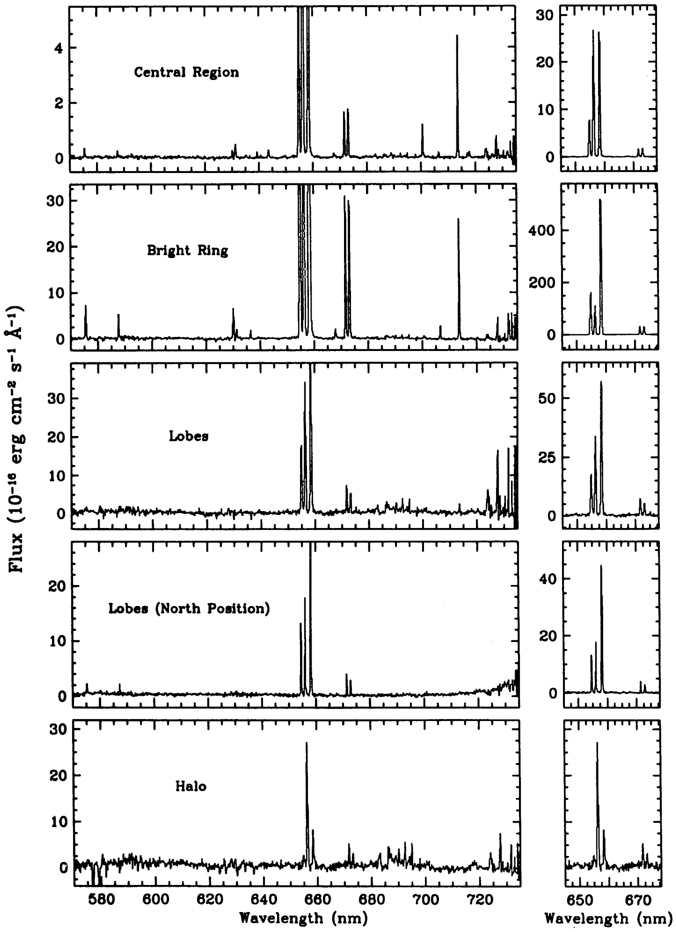

FIG. 7.—Red spectra of the different regions considered. [N II], Hα, and [S II] lines are shown separately.

reddening law of Whitford (1958). The extinction value is high ($c_{H\beta} = 1.31 \pm 0.05$), and no extinction differences higher than the error have been found in the different parts. The previous spectroscopic data (Acker et al. 1992) give $c_{H\beta} = 1.32$, in excellent agreement with our result. The dereddened line strengths from each region, related to Hα, are given in Table 2. An estimate of the errors involved in the flux measurements and the extinction coefficient calculation has been carefully derived.

5.2. *Electron Density and Temperature*

The electron density N_e was determined from the [S II] λ6717/λ6731 line ratio. The electron temperatures T_e were calculated from the [N II] (λ6584 + λ6548)/λ5755 line ratio for the low-excitation region and from the line ratio [O III] (λ4959 + λ5007)/λ4363 for the high-excitation region.

The derived electron densities and temperatures are listed in Table 3. Note that the electron density in regions CP, R, and N is almost constant (in region CP the value is highly uncertain, and we adopted that of adjacent region R for abundance calculations). The electron density determination in the halo and lobes is uncertain as well, because of proximity to the low-density limit (Stanghellini & Kaler 1989), and the calculation of N_e [S II] is very unreliable. We adopted a value for $N_e \sim 100$ cm^{-3}.

The electron temperature is almost constant too, within the uncertainty estimated. Where no electron temperature determination was possible, we assumed the same values inferred in region R for the abundance calculations.

5.3. *Chemical Abundances*

Once the electron density and temperature were derived for each region, the ionic abundances were computed from the line strengths using a program to solve the equations of statistical equilibrium for a five-level atom written by Preite-Martinez. We estimated the errors taking into account those associated with the line strength measurements and those due to the electron densities and temperatures calculations. The elemental abundances were calculated according to the standard formalism of ionization correction factors (Torres-Peimbert & Peimbert 1977). The ionic and elemental abundances and their errors are listed in Table 3. Errors involved in flux measurements, and electronic temperatures and density calculations, were considered in order to calculate abundance errors.

For inferring helium abundances, we corrected the He I lines for collisional effects (Clegg 1987). The attained values are very similar within the errors, so there does not seem to be a gradient in the helium abundance. The value obtained for regions CP, R, and N ranges between 0.14 and 0.17, which is a typical helium abundance for type I PNs (Peimbert & Torres-Peimbert 1982). To study the possible variations in the N/O ratio, we approximated this ratio by N^+/O^+, because the temperature dependences of N^+ and O^+ abundances virtually cancel each other. The most significant fact is that in the ring (R) the ratio found (N/O ∼ 4.2) is roughly five times that found in bipolar PNs (Corradi & Schwarz 1995). Despite the error associated to the N/O determination in this region, the high value seems to be real. In the central part (CP), the value is lower (2.4) but is affected by a large uncertainty. The north region (N) gave N/O ∼ 0.4. For the halo we only have information about the O^{++}/H^+ ratio, whereas a great part of oxygen should be present in lower ionization states. The ratio N^+/O^{++} is ∼0.4. Therefore, the halo seems to be nitrogen poor, since the ratio N/O should presumably be well below than this value.

6. ON THE DISTANCE TO K4-55

In order to determine the distance to K4-55, we profit from the fact that, as noted above, no differences higher than 0.05 in $c_{H\beta}$ appear to exist in the extinction throughout the nebula. So the optical extinction toward K4-55 is fundamentally caused by interstellar dust and is not associated to absorbing dust inside the object.

Under this assumption, we can derive the distance using the reddening-distance method established by Lutz (1973). This method is based on the relationship between interstellar reddening and distance for field stars close to the line of sight of the PN. This relation requires precise photometric and spectroscopic data of the stars to determine their magnitudes, colors, spectral types, and luminosity classes. We obtained these data from the SIMBAD data base of the Astronomical Data Center in Strasbourg, France. The most precise photometric data have been compiled for stars whose spectral type and luminosity classes are determined unambiguously and whose angular distance to the position of the nebula is less than 45′. The data and the references of their origin are listed in Table 4. As this information is available for an adequate number of useful stars, we have not considered it necessary to obtain additional photometry of stars in a small field around K4-55. Even though this additional work may give us more

TABLE 2

DEREDDENED LINE INTENSITY RATIOS FOR K4-55

Line	$f(\lambda)$	CP		R		L		N		H	
λ3727 [O II]	+0.257	83	±33	170	±39	...		586	±127	...	
λ3750 H12	+0.253	...		97	±18	...		...		...	
λ3869 [Ne III]	+0.231	78	±30	113	±18	...		...		...	
λ4101 Hδ	+0.182	47	±18	57	±10	...		...		...	
λ4340 Hγ	+0.135	37	±6	45	±8	...		54	±29	...	
λ4363 [O III]	+0.129	10.7	±3.2	15.3	±3.6	...		...		...	
λ4686 He II	+0.043	85	±12	48	±5	...		16.2	±5.4	...	
λ4715 [Ne IV]	+0.036	23.8	±4.9	...		...		...		...	
λ4725 [Ne IV]	+0.033	5.7	±1.9	...		...		...		...	
λ4740 [Ar IV]	+0.030	14.4	±3.6	...		...		...		...	
λ4861 Hβ	0.000	100		100		100		100		100	
λ4959 [O III]	−0.024	214	±37	293	±20	79	±20	110	±21	113	±37
λ5007 [O III]	−0.030	657	±102	893	±53	246	±51	307	±41	289	±87
λ5199 [N I]	−0.083	5.7	±3.0	17.9	±2.5	...		...		...	
λ5755 [N II]	−0.205	7.7	±2.8	24.8	±2.5	...		11.6	±6.2	...	
λ5876 He I	−0.225	3.6	±1.7	14.1	±1.7	...		16.7	±6.0	...	
λ6300 [O I]	−0.298	3.7	±1.1	16.9	±1.7	...		5.5	±1.0	...	
λ6312 [S III]+He II	−0.299	8.5	±1.9	6.6	±0.9	...		1.9	±0.9	...	
λ6364 [O I]	−0.310	1.2	±0.4	4.8	±0.7	...		2.7	±0.9	...	
λ6406 He II	−0.313	1.4	±0.6	...		...		...		...	
λ6436 [Ar V]	−0.316	5.0	±1.3	...		...		...		...	
λ6548 [N II]	−0.338	121	±19	421	±25	164	±33	143	±17	44	±14
λ6563 Hα	−0.340	409	±59	282	±17	285	±56	255	±39	293	±87
λ6584 [N II]	−0.343	398	±58	1373	±80	506	±99	480	±57	97	±29
λ6678 He I	−0.353	2.5	±0.7	4.6	±0.6	...		2.7	±2.0	...	
λ6683 He II	−0.354	1.2	±0.4	...		...		2.7	±2.0	...	
λ6717 [S II]	−0.362	22.4	±3.9	72	±5	58	±12	40	±6	54	±16
λ6731 [S II]	−0.364	24.5	±4.2	71	±5	38	±8	38	±5	29.4	±9.2
λ7008 [Ar V]	−0.380	14.0	±2.6	...		...		4.2	±1.6	...	
λ7065 He I	−0.387	2.3	±0.8	5.9	±0.6	...		2.6	±0.4	...	
λ7137 [Ar III]	−0.396	39	±6	38.8	±2.6	11.7	±2.9	15.6	±2.3	...	
λ7170 [Ar IV]	−0.400	1.7	±0.6	...		...		...		...	
λ7178 He II	−0.400	3.3	±0.9	...		...		...		...	
λ7230 [O II]	−0.419	2.7	±0.9	5.4	±0.5	...		...		...	
λ7330 [O II]	−0.419	3.7	±1.2	5.5	±0.6	...		...		...	
F(Hβ)[a]		28.2		167.0		52.7		34.8		40.2	

[a] Dereddened flux in units of 10^{-15} ergs $\mathrm{cm}^{-2}\ \mathrm{s}^{-1}$.

reliable distances (Gathier, Pottasch, & Pel 1986), such photometric work would exceed the scope of our study of K4-55.

For a given star, the color excess was calculated from the observed $(B-V)$ and the intrinsic $(B-V)_0$. We used a ratio of visual extinction to reddening depending on the spectral energy distribution and on the reddening (Olson 1975):

$$A_v = [3.25 + 0.25 \times (B-V)_0 + 0.05 \times E_{B-V}] \times E_{B-V} . \quad (2)$$

To obtain the distance to each star, we derived the corresponding distance modulus from the corrected apparent magnitude and the absolute magnitude. The intrinsic $(B-V)_0$ and the absolute magnitude were both taken from the compilation by Schmidt-Kaler (1982). BZ Cyg is a classical Cepheid with a period of 10.14 days, so the reddening and distance were calculated using appropriate intrinsic $(B-V)_0$ and absolute magnitude for this type of star (Duerbeck & Seitter 1982). The results appear in Figure 8, where A_v has been plotted against distance for all the stars considered. Most of the stars are closer than 1 kpc and have $A_v \leq 2$. BZ Cyg provides a crucial piece of information on this plot, and since it is a classical Cepheid, we believe its distance and reddening are very reliable.

In addition, plotted in Figure 8 are the reddening distributions by Lucke (1978), based on the compilation of photometry and spectroscopy data for O and B stars within 1 kpc of the Sun and 100 pc from the Galactic plane (*short-dashed line*), and within 2 kpc of the Sun and 200 pc from the Galactic plane (*dot-dashed line*). Comparison between both lines shows that once the edge of the Galactic disk is reached ($z \sim 140$ pc), the extinction increases very slowly with distance, revealing a plateau such that the stars are located in regions over the Galactic disk which contain little dust.

Our fit to the data points is also shown in Figure 8. The reddening distance fit was weighted with the errors in the photometric and distance determinations and with the angular distance between each of the stars and the nebula. According to this relation, a value of 3.0 mag for A_v in K4-55 means a distance of 1.4 kpc. The associated error was estimated to be greater than 200 pc. We must be very careful when comparing this result with Lucke's curves. The dust distribution in the Cygnus region of the Galactic plane ($60° \lesssim l \lesssim 90°$) is very patchy and shows structure on a scale of less than 1°. As the curves obtained by Lucke represent values of extinction averaged over wide fields, our estimate states more accurately the reddeningdistance relation in this direction.

We have also estimated the distance using the Shklovsky method, despite the fact that it generally provides very inaccu-

TABLE 3

PHYSICAL CONDITIONS AND CHEMICAL ABUNDANCES

		CP		R		L		N		H	
n_e [S II]		800[a]		500	$\pm^{200}_{300}$	100[b]		450	±150	100[b]	
T_e [N II]		10500	± 750	10500	± 750	10500[b]		10500[b]		10500[b]	
T_e [O III]		14000	±1500	14000	±1500	14000[b]		14000[b]		14000[b]	
O^{++}/H^+	$\times 10^5$	8.7	±2.5	11.8	±2.5	3.3	±1.1	4.1	±1.1	3.8	±1.6
O^+/H^+	$\times 10^5$	2.8	±1.0	5.7	±1.8	...		20.	±8.	...	
O^0/H^+	$\times 10^6$	6.5	±2.0	27.	±7.	...		12.	±3.	...	
O/H	$\times 10^5$	24.0		24.0		...		27.		...	
N^+/H^+	$\times 10^5$	6.7	±1.9	23.3	±5.0	8.6	±2.7	8.1	±2.1	1.6	±0.6
N/H	$\times 10^4$	5.8		10.0		...		1.1		...	
S^+/H^+	$\times 10^6$	1.1	±0.3	3.2	±0.7	1.9	±0.6	1.8	±0.6	1.7	±0.7
S/H	$\times 10^6$	9.9		8.4		...		6.2		...	
Ar^{4+}/H^+	$\times 10^6$	2.0	±0.4	...		...		0.6	±0.2	...	
Ar^{+++}/H^+	$\times 10^6$	2.4	±0.8	...		...		...		...	
Ar^{++}/H^+	$\times 10^6$	1.8	±0.4	1.7	±0.3	0.5	±0.2	0.7	±0.2	...	
Ar/H	$\times 10^6$	6.2		3.3		...		...		...	
Ne^{++}/H^+	$\times 10^5$	1.9	±0.9	2.8	±0.9	...		...		...	
Ne/H	$\times 10^5$	4.0		5.4		...		...		...	
He^+/H^+	(5876)	0.028	±0.016	0.113	±0.022	...		0.134	±0.05	...	
He^+/H^+	(6678)	0.065	±0.025	0.121	±0.026	...		...		...	
He^+/H^+		0.047		0.118		...		0.134		...	
He^{++}/H^+	(4686)	0.093	±0.03	0.053	±0.01	...		0.018	±0.01	...	
He/H^+		0.14	±0.04	0.17	±0.02	...		0.15	±0.05	...	
N^+/O^+		2.4	$\pm^{2.0}_{1.0}$	4.2	$\pm^{2.7}_{1.5}$	...		0.4	$\pm^{0.3}_{0.2}$	...	
Ne/O		0.22		0.24		...		...		...	

[a] As the uncertainty in this value is very high, we adopted 500 cm^{-3}.

[b] Assumed values.

rate individual distances, because it makes use of mean values for any properties of PNs that could change roughly from one to another. Using the recent calibration reported by Cahn, Kaler, & Stanghellini (1992) and Acker et al.'s (1991) $F_{H\beta}$ value, we obtained 2.6 kpc, nearly twice our distance estimate. Using the rotation curve of the Galaxy of Sellwood & Sanders (1988) and the radial velocity (LSR) found previously, we deduce a kinematic distance $\lesssim 2$ kpc, consistent with the 1.4 kpc value that we will adopt as the distance to the nebula.

7. DISCUSSION

7.1. *Bipolar Expansion*

As noted above, the velocity-position plot extracted from the echelle spectrum oriented in the E-W direction shows the usual characteristics of bipolar expansion. Two pairs of features appear outside the bright central region (see [N II] echelle image in Fig. 3 [*top*]), the more extended reaching up to 40″, related in such a way that, if one is redshifted on one side, the

TABLE 4

LITERATURE DATA FOR STARS

Star	Spectral Type	Luminosity Class	m_v (mag)	$B-V$ (mag)	$U-B$ (mag)	A_v (mag)	d (pc)	References
SAO 50008	B9	V	8.97	+0.01	−0.04	0.27	500	1, 2, 3
HD 197391	B8	V	9.09	+0.03	+0.02	0.46	600	1, 3
SAO 50024	A0	IV	9.50	+0.14	+0.08	0.54	540	1, 2, 3
CSI +44-20438	B9	V	10.70	+0.31	+0.23	0.96	810	1
CSI +43-20460	B8	V	10.92	+0.37	+0.14	1.56	836	1
SAO 49996	A0	IV	8.86	+0.17	+0.15	0.64	380	1, 2, 3
CSI +44-20442	A0	V	11.93	+0.29	+0.14	1.06	1100	1
CSI +44-20456	B7	V	10.40	+0.41	+0.07	1.72	720	1
CSI +43-20458	A0	V	12.12	+0.39	+0.18	1.39	910	1
SAO 49986	B7.5	V	8.63	−0.08	−0.35	0.14	410	1, 2, 3
SAO 49982	A0	V	9.54	+0.04	−0.01	0.18	363	1, 2
SAO 49997	A6	IV	9.81	+0.04	...	0.14	430	2, 4
BD +44 3569	A7	V	8.71	+0.01	...	0.04	248	2
BD +43 3721	B9	V	10.34	+0.24	+0.13	1.01	670	1
CSI +44-20454	B9	V	11.13	+0.42	+0.26	0.44	660	1
BD +44 3554	G7	III	8.52	+0.08	...	0.27	195	2
BD +44 3559	A2	V	10.03	+0.11	...	0.36	358	2
BD +44 3581	A5	V	9.18	+0.10	...	0.32	236	2
BZ Cyg	F8	Ib	10.22	+1.60	...	3.42	1500	5

REFERENCES.—(1) Bigay & Garnier 1979, (2) Straizys et al. 1989, (3) Fehrenbach et al. 1961, (4) Lacroute & Valbousquet 1971, (5) Szabados 1981.

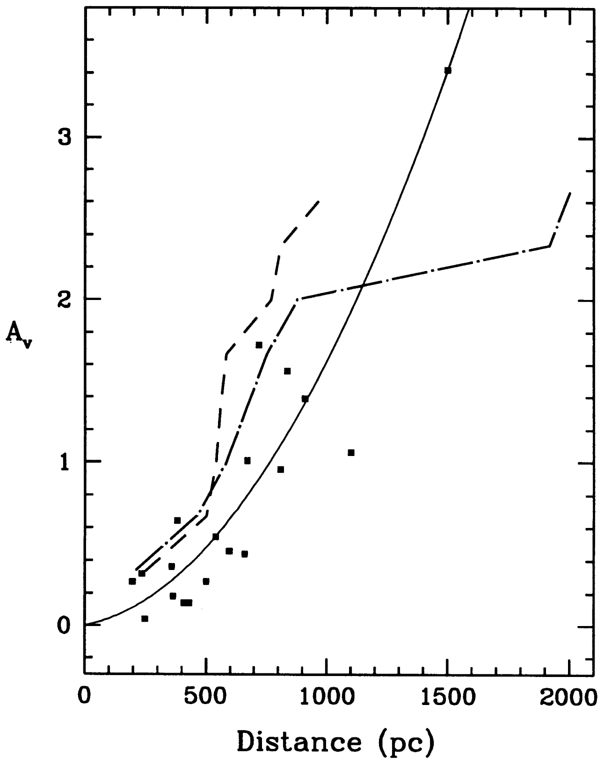

FIG. 8.—Extinction vs. distance plot in the direction of K4-55. Filled squares correspond to the compilation of published photometric data for stars closer than 45′ to the nebula. The short-dashed and dot-dashed lines denote the fits by Lucke (1978) based on data for O and B stars in the same direction within 1 and 2 kpc from the Sun, respectively. The solid line is our fit to the data. The calculated extinction for K4-55, $A_v = 3.0$ mag, corresponds roughly to a distance of 1400 pc.

pair is blueshifted on the other side of the central nebula. In order to establish the inclination of the bipolar structure, we have considered that the position of the E-W oriented slit is almost coincident with the projection onto the sky of the axis of symmetry of this object. The image through the Hα + [N II] filter seems to confirm that, if there were any difference, it would be negligible. Figure 9 (*left*) shows a two-dimensional scheme of the geometry proposed for this nebula. Using the simple model of a bipolar expanding nebula (Solf & Ulrich 1985),

$$V_{\rm exp}(\phi) = V_e + (V_p - V_e)|\sin \phi|^{\gamma} , \qquad (3)$$

where ϕ is the latitude angle, varying from 0° at the equator to 90° at the poles; V_e and V_p are the equatorial and polar velocities; and γ is a shape parameter. Figure 9 (*center*) shows that there is excellent agreement with our observational data (see Fig. 9 legend). The velocity at the pole was estimated to be 100 ± 10 km s^{-1} and the inclination to be $20° \pm 5°$. According to our interpretation, this nebula is a bipolar PN seen near pole-on. The uncertainties in using this simple model and in the exact orientation of the projection onto the sky of the axis of symmetry could affect these values, but the quality of the fit to the observational data would constrain the possible explanations to an outflow collimated in the direction above indicated.

In the S-N oriented long-slit we are seeing the lobe that moves away through the approaching lobe, which explains the line-splitting observed. The extension of the emission is lower than in the E-W long slit because the projection on the sky of the axis of symmetry is almost perpendicular to the S-N direction. The assumed model reproduces well the data in this position (Fig. 9 [*right*]).

A last attempt to confirm the geometry of the bipolar structure of K4-55 has driven us to elaborate a synthetic sky-projected image in order to compare it with the Hα + [N II] image. We considered a hollow bipolar structure in which the material is deposited on thin walls, whose thickness is 10% of

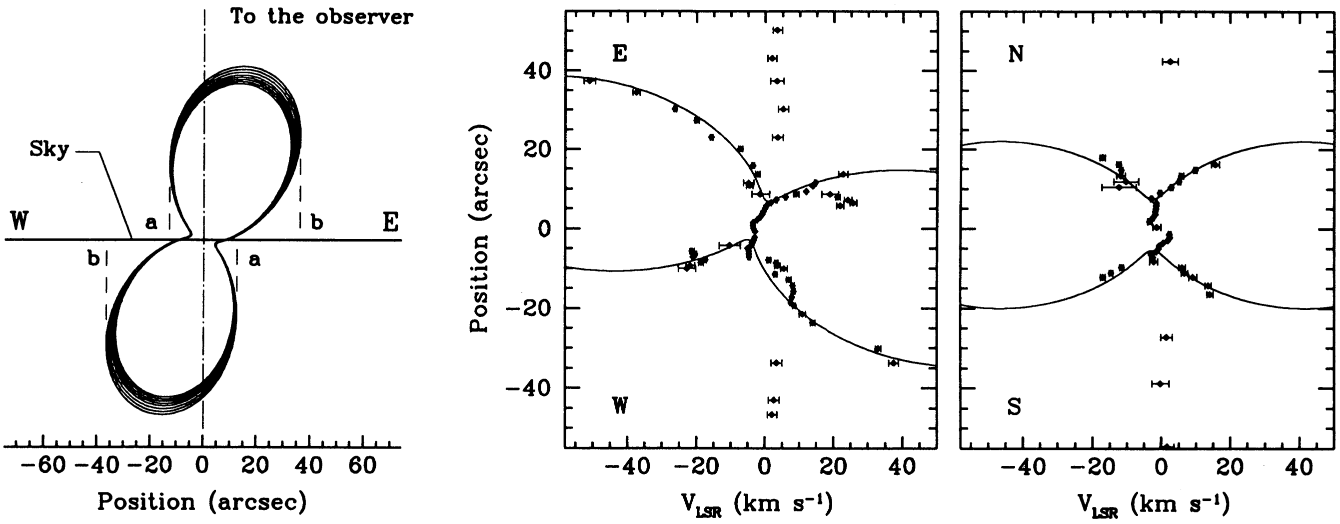

FIG. 9.—*Left:* Sketch of the geometry proposed for the nebula and velocity fit to the original data. A schematic draft of the positioning proposed for the lobes of K4-55 in a section through the center of the nebula in E-W direction. The inclination is 20°, and the model is the same as that explaining the velocity field. Points a are the projection on the plane of the sky of the armlike structures, whereas points b represent the maximum extension of the projected lobes. In the center, we show the velocity field modelization fit to the data of K4-55 through the E-W–oriented slit, according to Solf & Ulrich's (1985) model with $\gamma = 2.5$, $V_p = 100$ km s^{-1} and $V_e = 8$ km s^{-1}. The same fit is shown on the right, but applied to the slit position through the N-S direction. The model is the same, and there is enough agreement.

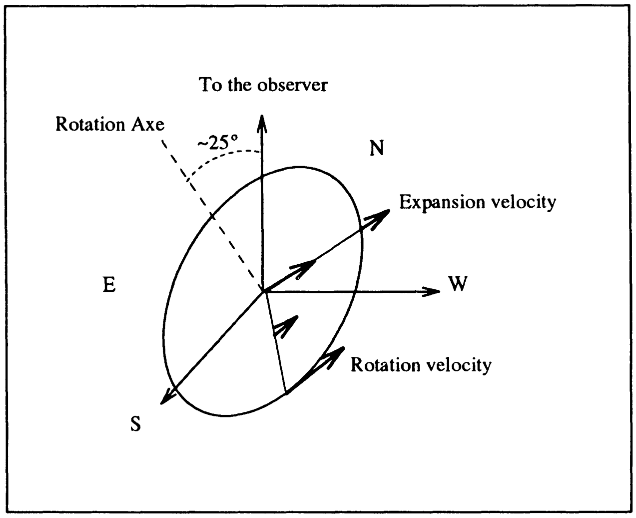

FIG. 11.—Sketch of the geometry proposed for the inner part of the nebula. Material is placed on a disk or torus whose rotation axis is inclined 25° in the S-N direction. Expansion and rotation velocities have been shown schematically as arrows. The expansion velocity is higher as we move toward the center, whereas the rotation velocity is higher at the edge.

the distance to the center. The emission at each point has been modeled as a decreasing function of a power of the distance to the center ($r^{-\xi}$). Rough estimates for different values of the inclination angle and the exponent ξ are shown in Figure 10 (Plate 25). The synthetic images have been degraded according to the observational conditions (seeing and read-noise features of the chip) to allow a fair comparison. The inclination angle is in good agreement with the value calculated from the kinematic observations (~20°), while the emission breaks off, the exponent ξ being as high as 2.5. It is unclear whether this effect is due to decreasing the electron density, which would affect the Hα emission especially, since our image contains not only this line but also [N II] emission, which is also affected by changes in electron density, but is strongly modified by changes in electron temperature and abundance. Caution must be taken when comparing our very simple models with the emission of this nebula. At all events, it is a fact that the emission at the end of the lobes is very faint or even nonexistent.

We may conclude that the projection of this geometry over the plane of the sky fits qualitatively the outer features of the morphology of the nebula as the bipolar lobes. The armlike features that are point-symmetric in the outside of the central ring (Fig. 3) are then moving in opposite directions, and they are really limb-brightened, because we are looking through the edge of the lobes. Assuming a distance of 1.4 kpc to the nebula and a velocity expansion of 100 km s^{-1}, we obtained a linear size of 0.9 pc and a dynamical age of 4300 yr for the lobes.

7.2. *Kinematics of the Inner Part*

As presented in § 4, the central part of this object (12″ × 10″ in size) shows a peculiar behavior. Its kinematical properties suggested that we might be seeing rotation, so we elaborated a simple kinematical model in which the material is placed over a flat disk that is rotating and expanding simultaneously. A sketch is shown in Figure 11. We assumed a rigid body law for the rotation, whereas the expansion was taken to be faster in the innermost part and slower toward the edges of the disk. Comparison between the original and synthetic data gives a reasonable fit (Fig. 12), the rotation period being about 15,000 yr. The disk is inclined ~25° in the S-N direction and ~5° in the E-W direction, whereas the outer bipolar structure is bent in the E-W direction at an angle near 20°. Therefore, precession seems to exist between the inner and outer structures. The humpback in the velocity-position plot in the E-W slit orientation is explained by a small offset (~1″) in the slit position from the true center. This offset also introduces a small shift in

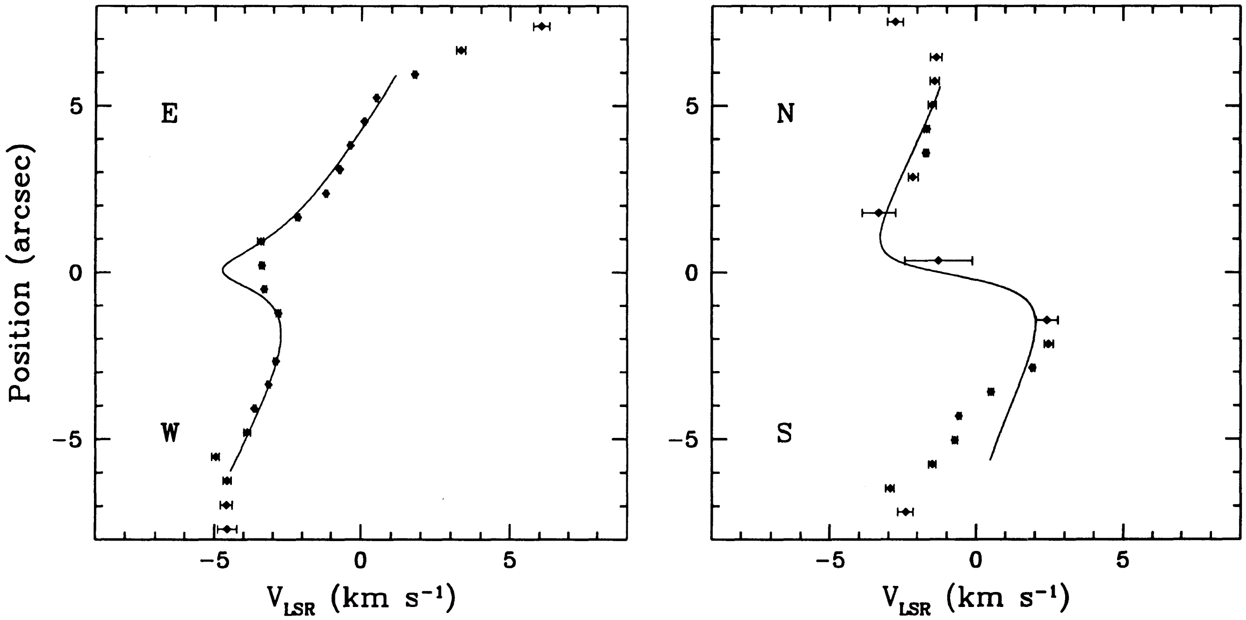

FIG. 12.—Fit to the original data of the model proposed. Velocity-position plot in the E-W oriented slit (*left*) and in the S-N direction (*right*). The reproduced data show the same trend as the original ones. However, the synthetic data do not follow exactly the same patterns, because there are too many parameters to fit from the available information (any possible offset in the position of the slit, the relationship between the expansion velocity modulus and radius on the disk, the exact law of rotation, etc.).

velocities, although our calculations reveal it to be negligible ($\lesssim 0.5$ km s^{-1}). The real structure of this emission region is probably not a disk but is more like a torus, according to the emission profile, which is very peaked on the bright ring, although some emission seems to be present at the center.

The specific angular momentum, J/M, of such a toroidal structure is $\sim 2 \times 10^{23}$ cm^2 s^{-1} (corresponding to an angular rotational velocity $\omega = 1.3 \times 10^{-11}$ s^{-1} and a radius of 3.7×10^{-2} pc or 1.1×10^{17} cm). The mass can be estimated using expression (V.7) from Pottasch (1984, p. 111):

$$M(M_\odot) = 11.06 F(\mathrm{H}\beta) t^{0.88} D^2 N_e^{-1} , \qquad (4)$$

where $F(\mathrm{H}\beta)$ is the flux in units of 10^{-11} ergs cm^{-2} s^{-1}, d is the distance in kpc, $t = T_e/10{,}000$ K, and N_e is the electron density in cm^{-3}. As only a fraction of the Hβ flux was measured, we multiplied it by a factor equal to the ratio of the total surface of the ring on the sky to the surface effectively observed. Using this value, which agrees with the value given by Acker et al. (1991), we infer a mass of $\sim 7 \times 10^{-4}$ $M_\odot$. Subsequently, the total angular momentum, J, is $\sim 3 \times 10^{53}$ cm^2 s^{-1}.

The expansion within the disk is in agreement with models that predict the presence of an equatorial disk or torus (Soker & Livio 1994) collimating the bipolar outflow in bipolar PNs. The velocity is higher in the innermost parts, where material is being blown up, and less so toward the edge of the disk or torus, where it accretes. However, rotation is more difficult to explain, as well as the likely precession between the collimating and collimated structures, but the presence of rotation and precession simultaneously might suggest a common cause. Since single star rotation cannot provide the angular momentum (Villata 1992) of the ring, an additional source should be considered. A plausible scenario would be an AGB star in a binary system going through a common envelope phase (Livio 1993). The spinning up of the AGB envelope star by the companion star causes the observed rotation (for a companion with 1 $M_\odot$ and an initial separation of 1 AU about a 5 $M_\odot$ primary, the J of the secondary coincides with that observed in the ring).

The previous discussion concerns the argued origin of bipolarity among PNs. Several mechanisms have been proposed: close companions (Livio 1993), magnetic fields (Morris 1987), or an interacting wind (Icke et al. 1989; Balick 1987). Although bipolar structures are a common phenomenon in PNs (Schwarz 1993), what causes them still remains unclear. The data presented in this work point to the existence of a rotating disk shaping K4-55, but, in the current status, it should be concluded that more information is needed. In particular, we have poor spatial information on these motions, and more high-resolution information at different positions in the bright central part of the nebula would be desirable.

7.3. *Chemical Abundances*

The N/O ratio reported in the ring (N/O = 4.2) is among the highest ever found in PNs (Henry 1990; Perinotto 1991). It is higher than in the central (CP) and outer parts (L, N, and H). The value found in the central region (CP) could be due to emission contamination from the lobes, because we are viewing the CP through the lobes that show a lower N/O ratio. The difference between the [N II] to [O II] line ratio in the ring and lobes is difficult to explain (it varies roughly by a factor 10), save as a result of enhancement of the nitrogen abundances in the ring. Because of the similar ionization potential of both ions, a change of temperature between the regions cannot be invoked. Since shock excitation is capable of producing an enhancement of the [N II] lines, it would be worthwhile to investigate it as an alternative explanation for the high N/O ratio found. For reasonable shock velocities and assuming solar nitrogen abundances (N/H $\sim 9.1 \times 10^{-5}$), planar shock models of Herbig-Haro objects (Hartigan, Raymond, & Hartmann 1987) cannot account for the nitrogen to Hα line ratio found in the bright ring ($I[\lambda 6584]/I[\mathrm{H}\alpha] \sim 4.8$). In addition, the λ6300 [O I] and λ5199 [N I] lines, which are very sensitive to the presence of shocks, do not show evidence of it (although they are more relevant than in the adjacent regions).

The chemical abundance indicates that the inner ring was formed during a different mass-loss episode, as opposed to the bipolar lobes. The high value found for the N/O ratio in the ring shows that the actual nucleosynthesis and dredge-up models, for intermediate-mass stars (Becker & Iben 1980; García-Berro & Iben 1994), fail to predict the surface abundance changes in AGB stars. Furthermore, it suggests that other mechanisms have to be taken into account when modeling the AGB phase. It also indicates that sudden mass-loss episodes take place during the post-AGB phase.

Iben & Tutukov (1995) predict such a high N/O value for a stellar evolution through a common envelope phase. Therefore, the chemical abundances of the central region, together with its former kinematic analysis, support the idea of a binary with a common envelope as the progenitor of the inner structure. However, no evidence of the central star or of binarity is found. We can only state that the presence of He II lines reveals a surface temperature, for the presumed progenitor star, at least higher than 45,000 K. On these grounds, the hypothesis of binarity cannot be directly confirmed.

7.4. *General Properties of the Halo*

The halo is static, and its spectrum is not due to reflection. This halo extends up to 4′, which means a large linear radius, over 0.8 pc at a distance of 1.4 kpc. It is not detected in the CCD images, thus indicating that it is very faint and that telescopes with greater apertures and/or narrower filters are needed to guarantee detection.

If instead of the electron density we introduce the filling factor, ϵ, in expression (4) as described in Pottasch (1984), the ionized mass can be calculated as

$$M(M_\odot) = 7.010^{-6} \times F(\mathrm{H}\beta)^{0.5} T_e^{0.44} D^{2.5} \theta^{2.5} \epsilon^{0.5} , \qquad (5)$$

where θ is the angular radius in arcseconds. To apply this expression, we first need to know the total Hβ flux. Assuming a model sphere for the halo, filled with gas at a constant density, the total Hβ flux was estimated from the flux measured over the slit, excluding the volume of the main nebula. Combining the value found (4.1×10^{-12} ergs cm^{-2} s^{-1}) with the distance and the assumed electron temperature, we obtained a mass over 0.75 $M_\odot$, when the filling factor is estimated as 0.85, which is the result of considering a filled sphere of radius 0.8 pc and subtracting the central volume taken up by the main nebula.

As estimated above, the expansion velocity is not higher than 8.6 km s^{-1}. Assuming that the expansion velocity is constant, we can calculate the dynamical age of the halo, which must be up to 9.3×10^4 yr, and the mass-loss rate during this phase, which is $\lesssim 8.1 \times 10^{-6}$ $M_\odot$ yr^{-1}. These values are in good agreement with those inferred for other extended PN halos, such NGC 6543 and NGC 6826 (Manchado & Pottasch 1989; Bryce et al. 1992) and NGC 6751 (Chu et al. 1991).

8. CONCLUSIONS

We have studied the morphology, kinematics, and physical conditions and chemical abundances of the planetary nebula K4-55. We have estimated roughly the distance to this object, finding large discrepancies with previous values determined statistically.

From the kinematics we deduce a bipolar expansion for the main nebula with polar velocities of ~ 100 km s^{-1} and an inclination angle of $\sim 20°$ with respect to the line of sight. We have successfully identified this structure with the morphological features, the armlike structures of the object corresponding to the bipolar lobes viewed nearly pole-on. The inner ring exhibits intriguing kinematics, indicating a likely presence of rotation. The halo shows an expansion velocity lower than 8.6 km s^{-1}.

K4-55 is a new triple-shell PN exhibiting the effect of mass loss from the progenitor star in a complex way. The effect of different dredge-up processes through the different shells has been investigated and correlated with the dynamical ages of each shell, confirming that they correspond to various mass-loss episodes. The combination of chemical and kinematical information has allowed us to infer how the central star of this nebula evolved. First, a steady wind during the AGB phase, lasting 10^5 yr, formed the halo which presents poorly processed material, the N/O ratio being very low. Subsequently, this may be associated to the ascension on the AGB phase. A superwind phase, which began at least 4000 yr ago, brought processed material to the nebula, shaping the lobes. Their N/O ratios and helium enrichment would correspond to the second dredge-up. Later, a sudden mass-loss episode took place, ejecting highly nitrogen enriched material from the stellar surface. Although a sequence in the evolution of the central star has been inferred, it must be stated that single intermediate-mass star nucleosynthesis models currently available fail to reproduce the observed abundances.

The IAC80 is operated on the island of Tenerife by the Instituto de Astrofisica de Canarias in the Spanish Observatorio del Teide. The 4.2 m William Herschel Telescope and 2.5 m Nordic Optical Telescope are operated on the island of La Palma by the Royal Greenwich Observatory and the Lund Observatory, respectively, in the Spanish Observatorio del Roque de los Muchachos of the Instituto de Astrofisica de Canarias. We thank Enrique García-Berro, Luis Cuesta, and Antonio Mampaso for helpful discussions. The authors wish to thank the referee for several comments which have improved the readability of the manuscript. We are also grateful to Andrea Preite-Martinez for the use of his program on abundance calculations and to Monica Murphy who read the manuscript. This research was partially funded through grant PB90-0570 from the Dirección General de Investigación Científica y Técnica of the Spanish Ministerio de Educación y Ciencia.

REFERENCES

Acker, A., Marcout, J., Ochsenbein, F., Stenholm, B., Tylenda, R., & Schohn, C. 1992, in The Strasbourg-ESO Catalogue of Galactic Planetary Nebulae, Part II (Garching: European Southern Observatory), 301
Acker, A., Stenholm, B., Tylenda, R., & Raytchev, B. 1991, A&AS, 90, 89
Balick, B. 1987, AJ, 94, 671
Balick, B., Gonzalez, G., Frank, A., & Jacoby, G. 1992, ApJ 392, 582
Becker, S. A., & Iben, I., Jr. 1980, ApJ, 237, 111
Bigay, J. H., & Garnier, R. 1979, A&AS, 1, 15
Brocklhurst, M. 1971, MNRAS, 153, 471
Bryce, M., Meaburn, J., Walsh, J. R., & Clegg, R. E. S. 1992, MNRAS, 254, 477
Cahn, J. H., Kaler, J. B., & Stanghellini, L. 1992, A&AS, 94, 399
Chu, Y.-H., Jacoby, G., & Arendt, R. 1987, ApJS, 64, 529
Chu, Y.-H., Manchado, A., Jacoby, G., & Kwitter, K. 1991, ApJ, 376, 150
Clegg, R. E. S. 1987, MNRAS, 229, 31p
Corradi, R. L. M., & Schwarz, H. E. 1995, A&A, 293, 871
Duerbeck, H. W., & Seitter, W. C. 1982, in Landolt-Börnstein, Numerical Data and Functional Relationships in Science and Technology, NS, Vol. 2b, ed. K. Schaifers & H. H. Voigt (New York: Springer), 197
Fehrenbach, C., Petit, M., Cruvellier, G., & Peyrin, Y. 1961, J. Obs., 44, 233
García-Berro, E., & Iben, I. 1994, ApJ, 434, 599
Gathier, R., Pottasch, S. R., & Pel, J. W. 1986, A&A, 157, 171
Hartigan, P., Raymond, J., & Hartmann, L. 1987, ApJ, 316, 323
Henry, R. B. 1990, ApJ, 356, 229
Iben, I., & Renzini, A. 1983, AR&A, 21, 271
Iben, I., & Tutukov, A. 1995, preprint
Icke, V., Preston, H. L., & Balick, B. 1989, AJ, 97, 462
Jewitt, D. C., Danielson, G. E., & Kupferman, P. N. 1986, ApJ, 302, 727
Kohoutek, L. 1972, A&A 16, 291
Lacroute, P., & Valbousquet, A. 1971, in IAU Colloq. 7, AGK3 Catalogue, ed. W. J. Luyten (Minneapolis: Univ. of Minnesota), 153
Livio, M. 1993, in Circumstellar Media in the Late Stages of Stellar Evolution, ed. R. E. S. Clegg, I. R. Stevens, & W. P. S. Meikle (Cambridge: Cambridge Univ. Press), 35
Lucke, P. 1978, A&A, 64, 367
Lutz, J. H. 1973, ApJ, 181, 135
Manchado, A., Guerrero, M. A., Kwitter, K., & Chu, Y.-H. 1993, BAAS, 24, 1227
Manchado, A., Guerrero, M. A., Stanghellini, L., & Serra-Ricart, M. 1996, in preparation
Manchado, A., & Pottasch, S. R. 1989, A&A, 222, 219
Morris, M. 1987, PASP, 99, 115
Olson, B. I. 1975, PASP, 87, 349
Peimbert, M., & Torres-Peimbert, S. 1982, in IAU Symp. 131, Planetary Nebulae, ed. D. R. Flower (Dordrecht: Kluwer), 233
Perinotto, M. 1991, ApJS, 76, 687
Pottasch, S.R. 1984, Planetary Nebulae (Dordrecht: Reidel)
Sabbadin, F. 1986, A&AS, 65, 301
Schmidt-Kaler, Th. 1982, in Landolt-Börnstein, Numerical Data and Functional Relationships in Science and Technology, NS, Vol. 2b, ed. K. Schaifers & H. H. Voigt (New York: Springer), 1
Schwarz, H. E. 1993, in Mass Loss on the AGB and Beyond, ed. H. E. Schwarz (Garching: ESO), 223
Sellwood, J. A., & Sanders, R. H. 1988, MNRAS, 233, 611
Soker, N., & Livio, M. 1994, ApJ, 421, 219
Solf, J., & Ulrich, H. 1985, A&A, 148, 274
Stanghellini, L., & Kaler, J. B. 1989, ApJ, 343, 811
Straizys, V., Meistas, E., Vansevicius, V., & Goldberg, E. P. 1989, Vilnius Astron. Obs. Biul., 83, 3
Szabados, L. 1981, Comm. Konkoly Obs., 77
Torres-Peimbert, S., & Peimbert, M. 1977, Rev. Mexicana Astron. Astrofis., 2,181
Vassiliadis, E., & Wood, P. R. 1993, ApJ, 413, 641
Villata, M. 1992, MNRAS, 257, 450
Whitford, A.E. 1958, AJ, 3, 01